

Validated Numerical Model and Simulation-Based Design Optimization of a Photoacoustic Cell

Á. Csókási^{1,2,*}, P. Véghe^{1,2}, I. Magashegyi^{1,3,4}, Z. Bozóki^{1,2,3}

1. Centre of Excellence for Interdisciplinary Research, Development and Innovation of the University of Szeged, Szeged, Hungary.

2. Department of Optics and Quantum Electronics, University of Szeged, Szeged, Hungary.

3. HUN-REN-SZTE Research Group for Photoacoustic Monitoring of Environmental Processes, Szeged, Hungary.

4. Department of Theoretical Physics, University of Szeged, Szeged, Hungary.

Abstract

Photoacoustic spectroscopy (PAS) enables highly sensitive gas detection without optical detectors by directly measuring the sound generated from light absorption. However, the performance of PAS systems strongly depends on the photoacoustic cell's acoustic design. In this work, we developed a three-dimensional finite element model of a differential longitudinal photoacoustic resonator using COMSOL Multiphysics 6.3 and the Acoustics Module. The model was built with the Pressure Acoustics, Frequency Domain interface, including resonators, buffer volumes, and microphones represented by impedance boundary conditions. A frequency domain study yielded the resonance curve, which matched well with experimental measurements, validating the model. Based on this, we performed a simulation-based design optimization, varying buffer dimensions to study their effect on the signal-to-background ratio (SBR). As the changes targeted only the buffer volumes, significant variations in the Q-factor were not expected; however, SBR could be improved by reducing the background signal originating from background processes such as laser–window interactions. The workflow demonstrates the potential of COMSOL Multiphysics® to design more efficient photoacoustic sensors and reduce prototyping iterations.

Keywords: Photoacoustics, Differential Resonator, Finite Element Model, Signal-to-Background Ratio (SBR), Design Optimization.

Introduction

The discovery of the photoacoustic (PA) effect in solids dates to 1880, when Alexander Graham Bell conducted experiments on long-distance sound transmission [1]. After Bell's pioneering work, it was recognized that the same effect could be observed in liquids and gases [2, 3]. However, following this initial excitement, further experiments were quickly limited by the available technology: the Sun was essentially the only light source, and the human ear served as the sole detector. Interestingly, even these early studies revealed the potential for resonant amplification of the generated PA signal by using an acoustic resonator. Nevertheless, for more than fifty years, photoacoustic spectroscopy (PAS) attracted little scientific attention. Practical applications of PAS for quantitative measurements only emerged in the 1930s. The literature first credits Mark Leonidovitch Veingerov in 1938 as the first to implement such a system [4]. The rise of measurements based on the PA effect began in the

late 1960s, when the development and broader use of lasers brought new possibilities for PAS, as it did in many other branches of spectroscopy [5]. Compared to conventional light sources, lasers offer outstanding beam quality and higher output power, which have proven crucial for enhancing sensitivity and enabling trace gas detection. Since the 1970s, the development of mid-infrared gas lasers (e.g., CO and CO₂ lasers) has also driven significant improvements in the detection sensitivity, compactness, and robustness of PAS systems [6]. The power of these gas lasers is in the order of a few watts, making them the perfect light source for detecting concentrations of ppb (parts per billion) and below. In the 1990s, diode lasers also proved to be excellent light sources due to their reliability and tunability [7]. More recently, novel laser technologies such as external cavity diode lasers, optical parametric oscillators based on periodically poled lithium niobate, and quantum cascade lasers have further expanded the possibilities for broadband and selective detection of trace gases [8, 9].

*Corresponding author.

E-mail address: csokasi.aron@szte.hu (Á. Csókási)

The key aspect of the PAS detection process is the amplification of the periodic pressure wave generated by modulated light absorption. This amplification is achieved by the acoustic resonator, known as the photoacoustic cell (PAC). When the frequency of the generated pressure wave coincides with one of the cell's resonant modes, strong acoustic amplification occurs due to constructive interference. Typically, such a cell is composed of one or two cylindrical tubes, each terminated with acoustic buffers that help reduce external acoustic noise and stabilize the resonance.

The dominant source of uncertainty in trace gas analysis arises from background noise contributions affecting the microphone signal. These background signals are primarily caused by interactions between the laser beam and the entrance and exit windows of the PAC [7, 10]. Such laser–window interactions can occur in two ways: through light scattering, where the transfer of photon momentum to the window surface induces mechanical vibrations that generate acoustic waves; and through absorption of light by the window material, which leads to localized heating and creates an additional PA source. Therefore, it is important to minimize the background signal already at the cell design stage.

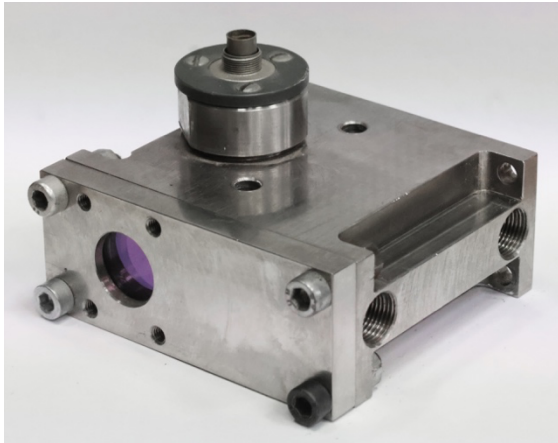


Figure 1. A photoacoustic chamber was developed by the Photoacoustic Research Group at the University of Szeged.

Numerous studies have reported experimental and theoretical investigations of gas PAC optimization. Baumann et al. (2006) were the first to apply the finite element method (FEM) modeling to the analysis of PACs. In their work, they simulated T-shaped cells consisting of a large-diameter cylinder, through which the laser beam propagated, and a narrow side branch containing a microphone that detected the amplified PA signal [11, 12]. Their FEM predictions showed reasonable agreement with experimentally measured frequency-dependent pressure amplitudes at the microphone position,

although the accuracy decreased at higher frequencies due to unaccounted thermoviscous effects. By contrast, later studies by Parvite et al. (2013) and Risser et al. (2015) demonstrated near-perfect agreement between FEM simulations and experimental data for the fundamental resonance mode of a differential Helmholtz cell [13, 14]. These results confirmed that FEM can accurately predict the acoustic behavior of PACs. Cotterell et al. (2019) noted that, although FEM has proven to be a reliable tool for predicting the acoustic behavior of PACs, previous studies did not systematically optimize cell design for maximizing the SBR, which fundamentally limits the detection capability of PAS [15]. Motivated by these results, we applied FEM modeling and optimization techniques to our existing chamber (Fig. 1).

Theoretical Background of PAS

The details of the PA effect have been derived by Rosencwaig and by Miklós, Hess, and Bozóki [16, 17]. Briefly, intensity-modulated laser light is absorbed by the sample, exciting molecular rotational, vibrational, or electronic energy levels. When collisional relaxation dominates the deactivation of these excited states, the absorbed energy is efficiently transferred to the translational motion of surrounding gas molecules. This transfer of energy results in local heating and thermal expansion, which in turn generates an acoustic pressure wave whose amplitude scales with the sample's absorption coefficient. A key aspect of the PA process is that this pressure wave can be amplified by exciting one of the photoacoustic cell's natural eigenmodes, forming a standing wave determined by the cell geometry. In resonant PAS, the laser modulation frequency is tuned to this resonance (eigenfrequency), thereby maximizing signal amplification.

The laws of fluid mechanics and thermodynamics can be applied to model the generation of sound waves. The governing physical equations are the conservation laws of energy, mass, momentum, and the thermodynamic equation of state. The physical quantities that describe the acoustic and thermal processes are the temperature T , pressure p , density ρ , and the three components of the particle velocity vector \mathbf{v} . From these, a linear wave equation can be derived for the pressure:

$$\nabla^2 p(\mathbf{r}, t) - \frac{1}{c^2} \frac{\partial^2 p(\mathbf{r}, t)}{\partial t^2} = -\frac{\gamma - 1}{c^2} \frac{\partial H(\mathbf{r}, t)}{\partial t}, \quad (1)$$

where c is the speed of sound, H is the heat density deposited by light absorption, and γ is the adiabatic coefficient. Taking the Fourier transform of

The cell was filled with a nitrogen–vapor water mixture, and we used the “Effective Material” setting node. The properties of the vapor water and nitrogen can be found in the Appendix Table 2.

The governing equations

The generated sound wave was calculated by the Helmholtz equation:

$$\nabla \cdot \left(-\frac{1}{\rho_c} (\nabla p - \mathbf{q}_d) \right) - \frac{\omega^2 p}{\rho_c c_c^2} = Q_m, \quad (9)$$

where ρ_c is the density, and c_c is the speed of sound in the medium. The “c” subscript refers to the word complex, because in lossy media these material properties can be modeled as complex-valued quantities (see below). The two sources Q_m and \mathbf{q}_d are the monopole source term and the dipole domain source, respectively. The latter one was set to zero. As for the Q_m monopole source, we used the “Heat source”, which adds a domain heat source that generates sound. This heat source represented the periodically varying heat distribution generated by the periodically modulated laser beam passing through Resonator A (Fig. 1). This condition is the following:

$$Q_m = \frac{\alpha_p}{\rho C_p} i\omega Q_{heat}, \quad \alpha_p = \frac{1}{c} \sqrt{\frac{C_p(\gamma - 1)}{T}}. \quad (10)$$

In this definition, α_p is the thermal expansion coefficient, C_p is the specific heat at constant pressure, and Q_{heat} is the power density. The power density’s spatial dependence was modeled with a Gaussian distribution:

$$Q_{heat}(\mathbf{r}) = \alpha_{mix} I_0 \exp\left(\frac{-2(y^2 + z^2)}{w_0^2}\right), \quad (11)$$

where

$$I_0 = \frac{P}{\iint_{S_w} \exp\left(\frac{-2(y^2 + z^2)}{w_0^2}\right) dS}. \quad (12)$$

The integral in the numerator was performed on the surface of the window (S_w). The absorption coefficient of the mixture, the beam radius, and the laser power were denoted by α_{mix} , w_0 , and P , respectively.

For the fluid model, we used the thermally conducting and viscous equivalent fluid model that mimics the propagation of sound, including losses due to thermal conduction and viscosity within the bulk of the fluid domain. These losses are defined as:

$$\rho_c = \rho \left(1 + \frac{i\omega\delta}{c^2}\right)^{-1}, \quad c_c = c \left(1 + \frac{i\omega\delta}{c^2}\right)^{\frac{1}{2}} \quad (13)$$

$$\delta = \frac{1}{\rho} \left[\left(\frac{4\mu}{3} + \mu_B \right) + \frac{(\gamma - 1)k}{C_p} \right], \quad (14)$$

where μ is the dynamic viscosity, μ_B is the bulk viscosity, and k is the thermal conductivity. This equivalent fluid model was employed to reduce computational cost while maintaining sufficient accuracy.

To consider the additional thermal and viscous losses occurring at the chamber wall using a boundary condition called “Thermoviscous Boundary Layer Impedance”. This boundary condition adds the losses due to thermal and viscous dissipation near the walls. The thickness of the viscous and thermal boundary layers is given by

$$\delta_v = \sqrt{\frac{2\mu}{\omega\rho}}, \quad \delta_{th} = \sqrt{\frac{2k}{\omega\rho C_p}}. \quad (15)$$

This boundary condition adds an impedance-like boundary condition by defining an inward normal velocity in terms of the pressure and its tangential component:

$$\mathbf{n} \cdot \left(\frac{1}{\rho_c} \nabla p \right) = -i\omega \mathbf{n} \cdot \mathbf{v}_{tv}, \quad (16)$$

$$-\mathbf{n} \cdot \mathbf{v}_{tv} = \frac{i\omega\alpha_p^2 T \delta_{th}}{\rho C_p (1+i)} p + \frac{\delta_v}{i\omega\rho(1+i)} \Delta_{\parallel} p. \quad (17)$$

The mechanical and thermal conditions with respect to this boundary condition were set to no-slip and isothermal, respectively. For all simulations, the input temperature and pressure were set to 80 °C and 1 atm, respectively, matching the experimental conditions applied during the validation measurements.

The MEMS microphones were modeled as impedance boundary conditions. This means that we defined a specific acoustic impedance boundary condition for the acoustic ports drawn in geometry:

$$\mathbf{n} \cdot \left(\frac{1}{\rho_c} \nabla p \right) = -p \frac{i\omega}{Z_M}, \quad (18)$$

where Z_M is the (normal) specific acoustic impedance of the microphones.

Model Validation with Measurements

To validate the FEM model, experimental measurements were performed on the actual PAC under the same conditions that were applied in the virtual space. The experimental setup consisted of a DFB laser with its driving electronics, a photoacoustic chamber, microphones, and a heating element used to maintain the cell at a constant temperature. The temperature needs to be increased to maintain the stability of the PA signal, as the resonance of the chamber depends on the temperature through the speed of sound. The schematic measurement setup is shown in Fig. 3. After selecting the appropriate absorption line of water vapor from the absorption spectrum ($\lambda = 1531.5$ nm), we recorded the resonance curve of the PAC in the range of 3–17.5 kHz with a step size of 12 Hz.

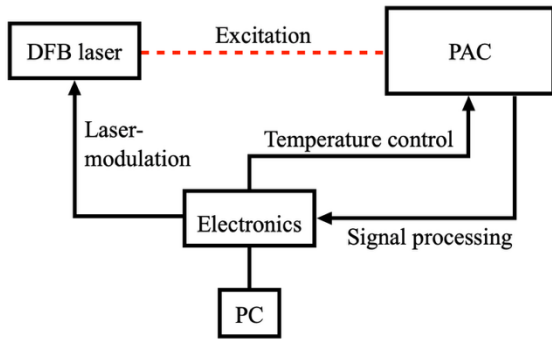


Figure 3. A schematic diagram of the measurement setup.

For comparison with the measurements, a Frequency Domain Study was performed in the numerical model, using the same frequency range and step size as in the experiments. The quantities of interest from the simulations are the complex acoustic pressures at the microphone positions, denoted as \mathbf{r}_{M_A} , and \mathbf{r}_{M_B} , corresponding to the names of the resonator tubes they are attached to. We calculated $p(\mathbf{r}_{M_A}, \omega)$ and $p(\mathbf{r}_{M_B}, \omega)$ by evaluating the pressure at the surfaces of the microphones' acoustic ports. Being complex-valued quantities, their real values can be either positive or negative, depending on the phase with respect to the equilibrium pressure. We defined the differential pressure signal as

$$p_{\text{diff}}(\omega) = p(\mathbf{r}_{M_A}, \omega) - p(\mathbf{r}_{M_B}, \omega). \quad (19)$$

The magnitude of these complex quantities gives the predicted microphone responses: $|p(\mathbf{r}_{M_A}, \omega)|$, $|p(\mathbf{r}_{M_B}, \omega)|$ and $|p_{\text{diff}}(\omega)|$. The results of the comparison are shown in Fig. 4, where the

differential signals from both the FEM and the measurements are plotted.

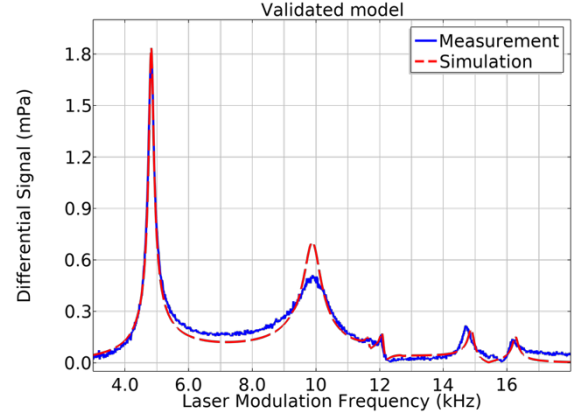


Figure 4. Measured and simulated (FEM) differential signal, showing good agreement in the examined frequency range.

Design optimization

In this section, we present a method for maximizing the detectable signal in terms of signal-to-background ratio (SBR). The background signal in this case is the acoustic sound generated by the laser-window interaction. These considerations are based on an article by Cotterell et al. (2019) [18].

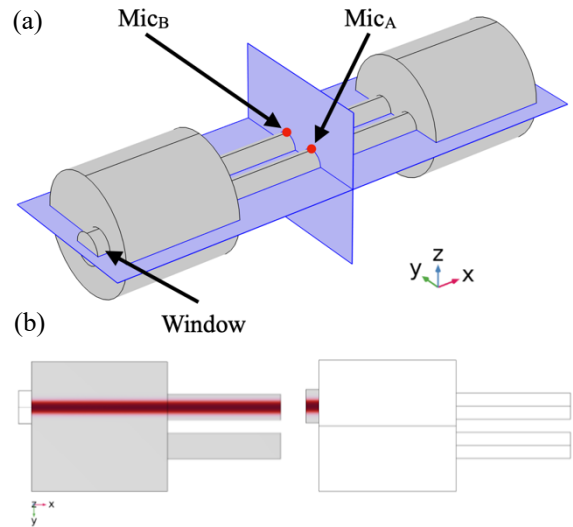


Figure 5. (a) The geometry used in the optimization. The blue planes represent the symmetry planes of the model, which reduced the running time. (b) The two heat source domains. On the left is the sample heating, while on the right is the window heating.

With the FEM model validated against the experiments, it became a reliable tool to optimize the geometry of the given PAC. For optimization, we chose the first resonance because this chamber operates within this frequency range. To maximize

the SBR at this resonance, we performed a parametric sweep on the radius and length of the buffer volumes. To calculate the SBR, we also need to consider the background processes. As mentioned earlier, the sound that emerges from background processes is most often a result of a laser–window interaction. Therefore, we introduced a heat source for the window heating domain, and the used geometry was simplified to the two buffer volumes and two resonator tubes. These window heating domains serve to localize the heat deposition within the PAC, in the vicinity of the window volume boundary. This heat deposition was also modeled by Eq. (11), except with the absorption coefficient of the window material (NBK-7, $\alpha_w = 0.83281 \text{ m}^{-1}$). The pressure was evaluated at the midpoint of the resonators. To reduce computational time, we utilized two symmetry planes (Fig. 5). We performed parametric sweep simulations for both sample and window heating. To calculate SBR, we calculated the differential signal generated by the sample and the window heating heat source domains. From Eqs. (3), (5), and (6), one can derive the modulus of the frequency response pressure as follows:

$$|p_{\text{diff}}(\omega)| = p_1 \sqrt{\frac{1}{1 + Q_1^2 \left(\frac{\omega_1}{\omega} - \frac{\omega}{\omega_1} \right)^2}}, \quad (20)$$

where p_1, Q_1, ω_1 are the fitting parameters, and the subscript “1” refers to the first resonance mode. Then, we defined the SBR as the ratio of p_1 fitted parameters for both heat source simulations:

$$SBR = \frac{p_1^{\text{sig}}}{p_1^{\text{bck}}}. \quad (21)$$

The appended superscripts “sig” and “bck” denote whether the excitation was provided by the sample (signal) and window (background) heating, respectively. We plotted the p_1 fit parameters with respect to the buffer length normalized by the resonator length in Fig. 6.

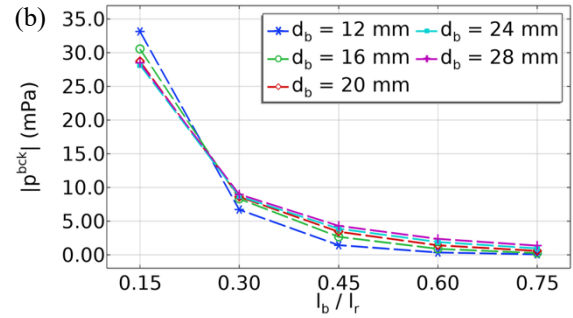
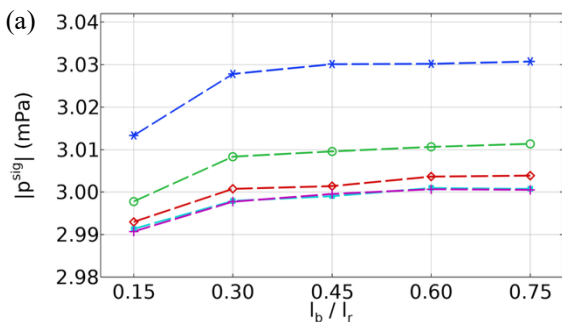


Figure 6. Changes in the fitted (a) p_1^{sig} (b) p_1^{bck} during variation of the buffer length. Different data series are shown for different buffer diameters. The lines are for illustrative purposes only.

Previous studies have shown that the ratio of buffers to resonators should be 0.5 for a one-resonator PA chamber [15, 19]. However, this relation does not apply to chambers with two resonators. Fig. 6a clearly demonstrates that signal generation by heating the trace gas is not sensitive to changes in the length or diameter of the buffer volumes. In contrast, the amplitude of the background signal is strongly affected by the buffer length: increasing its length significantly reduces noise caused by laser–window interaction. These phenomena can be explained as follows. Because of the attached resonators (via buffers), the chamber has two excitable modes between 4.5 kHz and 5.5 kHz. One of these modes, where the pressure is out of phase (ring mode), and where the pressure is in phase (longitudinal mode), which occurs within the resonator [20]. These modes can be visualized by plotting the pressure distribution (Fig. 7). The differential mode of the microphones amplifies the ring mode, while attenuating the longitudinal mode.

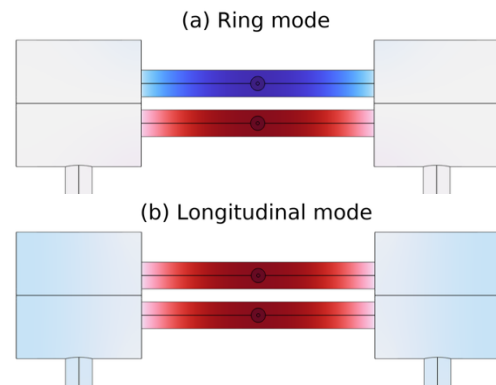


Figure 7. (a) The ring and (b) longitudinal modes in the frequency range of 4.5–5.5 kHz.

The heat source used for sample heating can effectively excite both modes, whereas window heating mainly excites the longitudinal mode. The decrease in the background signal is due to the so-

called phase manipulation. As already mentioned, the window heating is mainly exciting the longitudinal mode, in which case the pressure in the two resonators is in phase, so with the increase of the buffer length, such a geometry can be achieved, where the phase difference is nearly zero. This means that the differential operation mode of the microphones reduces the background signal.

From the fitted p_1^{sig} and p_1^{bck} parameters, one can calculate the SBR. In Fig. 8 we plotted the SBR with respect to the buffer length normalized with the resonator length for different buffer diameters.

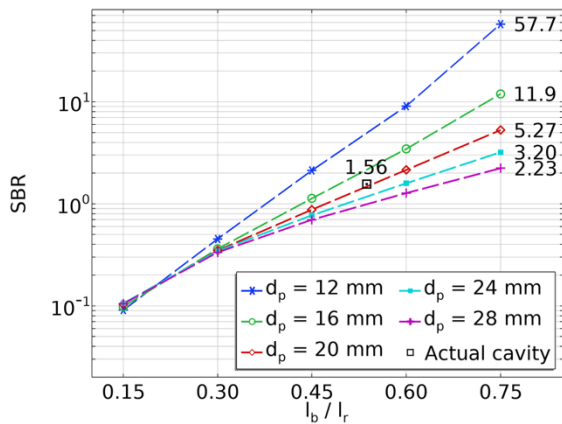


Figure 8. The signal-to-background ratio as a function of buffer length. The figure also contains data series corresponding to different buffer lengths, and the lines serve to facilitate the tracking of these data series.

Based on the design optimization, when $l_b = 0.75l_r$ and $d_b = 12$ mm, the chamber's signal-to-background ratio is 57.7. For comparison, the current SBR of the chamber is 1.56. This corresponds to an approximate 37-fold increase in SBR.

Conclusions

In this work, we developed and validated a 3D finite element model of a differential longitudinal photoacoustic cell using COMSOL Multiphysics®, Acoustics Module. The resonance behavior predicted by the model showed good agreement with experimental measurements, confirming its accuracy and reliability. The validated model was then applied to a geometry optimization study, focusing on buffer volume dimensions. The result demonstrated that the SBR can be significantly improved. The chamber's signal-to-background ratio can be increased from 1.56 to 57.7 by adjusting the buffer geometry: $l_b = 0.75l_r$ and $d_b = 12$ mm. These findings highlight the potential of FEM-based modeling and optimization to support the design of high-performance photoacoustic sensors while reducing the need for iterative prototyping.

Future work will extend the presented approach by incorporating thermoelastic effects to capture laser-window interactions in greater detail. Modeling heat deposition and mechanical response of the window material will enable a more realistic description of background noise processes. Additionally, experimental investigations will be carried out to directly measure the predicted background noise reduction, providing further validation of the model and supporting its application to practical photoacoustic sensor development.

References

- [1] A. G. Bell, "On the production of sound by light.," *American Journal of Science*, pp. 305-325, 1880.
- [2] J. Tyndall, "III. Action of an intermittent beam of radiant heat upon gaseous matter.," *Proceedings of the Royal Society of London*, vol. 31, no. 206-211, pp. 307-317, 1881.
- [3] W. C. Röntgen, "On tones produced by the intermittent irradiation of a gas.," *The London, Edinburgh, And Dublin Philosophical Magazine and Journal of Science*, vol. 11, no. 68, pp. 308-311, 1881.
- [4] M. L. Veingerov, "New method of gas analysis based on Tyndall-Röntgen optico-acoustic effect," *Dokl. Akad. Nauk SSSR*, vol. 19, pp. 687-688, 1938.
- [5] J. G. Atwood and E. L. Kerr, "The laser illuminated absorptivity spectrophone: a method for measurement of weak absorptivity in gases at laser wavelengths," *Applied optics*, vol. 7, no. 5, pp. 915-921, 1968.
- [6] M. W. Sigrist and S. Bernegger, "CO-laser photoacoustic spectroscopy of gases and vapours for trace gas analysis," *Infrared Physics*, vol. 30, no. 5, pp. 375-429, 1990.
- [7] Z. Bozóki et al., "A high sensitivity, near-infrared tunable-diode-laser-based photoacoustic water-vapour-detection system for automated operation," *Measurement Science and Technology*, vol. 10, no. 11, p. 999, 1999.
- [8] M. Gomes da Silva et al., "Photoacoustic measurement of N2O concentrations in ambient air with a pulsed optical parametric oscillator," *Applied Physics B*, vol. 82, pp. 329-336, 2006.

- [9] B. A. Paldus et al., "Photoacoustic spectroscopy using quantum-cascade lasers," *Optics letters*, vol. 24, no. 3, pp. 178-180, 1999.
- [10] D. A. Lack et al., "Aircraft Instrument for Comprehensive Characterization of Aerosol Optical Properties, Part 2: Black and Brown Carbon Absorption Enhancement Measured with Photo Acoustic Spectroscopy," *Aerosol Science and Technology*, vol. 46, no. 5, pp. 555-568, 2012.
- [11] B. Baumann et al., "Eigenmode analysis of photoacoustic sensors via finite element method," *Review of Scientific Instruments*, vol. 77, no. 4, pp. 044901-044901-6, 2006.
- [12] B. Baumann et al., "Finite element calculation of photoacoustic signals," *Applied Optics*, vol. 46, no. 7, pp. 1120-1125, 2007.
- [13] B. Parvitte et al., "Quantitative simulation of photoacoustic signals using finite element modelling software," *Applied Physics B*, vol. 111, no. 3, pp. 383-389, 2013.
- [14] C. Risser et al., "Optimization and complete characterization of a photoacoustic gas detector," *Applied Physics B*, vol. 118, no. 2, pp. 319-326, 2015.
- [15] M. I. Cotterell et al., "Optimizing the performance of aerosol photoacoustic cells using a finite element model. Part 1: Method validation and application to single-resonator multipass cells," *Aerosol Science and Technology*, vol. 53, no. 10, pp. 1107-1127, 2019.
- [16] A. Rosencwaig, *Photoacoustics and photoacoustic spectroscopy*, Chichester: Wiley, 1980.
- [17] A. Miklós et al., "Application of acoustic resonators in photoacoustic trace gas analysis," *Review of Scientific Instruments*, vol. 72, no. 4, pp. 1937-1955, 2001.
- [18] M. I. Cotterell et al., "Optimizing the performance of aerosol photoacoustic cells using a finite element model. Part 2: Application to a two-resonator cell," *Aerosol Science and Technology*, vol. 53, no. 10, pp. 1128-1148, 2019.
- [19] F. G. C. Bijnen et al., "Geometrical optimization of a longitudinal resonant photoacoustic cell for sensitive and fast trace gas detection," *Review of Scientific Instruments*, vol. 67, no. 8, pp. 2914-2923, 1996.
- [20] G. R. Lima et al., "Acoustic modeling and performance evaluation of 3D-printed and metal differential photoacoustic sensors for trace gas detection," *Measurement*, vol. 229, p. 114422, 2024.

Acknowledgements

This work was supported by the National Research, Development and Innovation Office (NKFIH), Hungary, under project *2024-1.2.3-HU-Rizont-2024-00031*, and by the Ministry for Innovation and Technology (ITM), Hungary, under project *ÉZFF/956/2022-ITM_SZERZ*.

Appendix

Table 1: Geometrical parameters and its values in mm.

Parameter - description	Value
Buffer length - l_b	18.9
Buffer diameter - d_b	19.1
Resonator length - l_r	35.2
Resonator diameter - d_r	4.00
Resonator separation - D_r	6.00
Filter length - l_f	17.4
Filter diameter - d_f	4.00
Connector length - l_c	45.0
Drill hole length- l_{DH}	3.00
Drill hole diameter - d_{DH}	1.40
Acoustic port diameter - d_{AP}	0.50
Helmholtz (H.) resonator diameter - d_H	2.15
H. resonator neck length - h_1	2.70
H. resonator volume height - h_2	1.50

Table 2: Material properties used in the Effective Material node.

	N₂	H₂O
M (g/mol)	28.0134	18.0153
c (m/s)	383.17	472.89
ρ (kg/m ³)	0.96518	0.62603
C_p (J/kg·K)	1042.7	2085.7
μ (10^{-5} Pa·s)	2.0275	1.25
μ_B (10^{-5} Pa·s)	1.3517	0.83
k (W/m·K)	0.029725	0.024705

Table 3: Physical parameters used in the Pressure Acoustics interface.

Parameter - description	Value
Laser power - P	79.6 mW
Beam radius - w_0	1.2 mm
Sensitivity of mic. "A" - S_A	-40 dB
Sensitivity of mic. "B" - S_B	-41 dB
Acoustic impedance of mics. - Z_M	10^6 Pa·s/m